Regime Switch in the Dual-Catalyzed Coupling of Alkyl Silicates with Aryl Bromides

Khaoula Jaouadi, Mehdi Abdellaoui, Etienne Levernier, Pierre-adrien Payard, Etienne Derat, Thomas Le Saux, Cyril Ollivier, Stéphane Torelli, Ludovic Jullien, Raphaël Plasson, et al.

▶ **To cite this version:**

Khaoula Jaouadi, Mehdi Abdellaoui, Etienne Levernier, Pierre-adrien Payard, Etienne Derat, et al.. Regime Switch in the Dual-Catalyzed Coupling of Alkyl Silicates with Aryl Bromides. Chemistry - A European Journal, 2023, 29 (59), pp.e202301780. 10.1002/chem.202301780 . hal-04245765

HAL Id: hal-04245765
https://hal.inrae.fr/hal-04245765

Submitted on 17 Oct 2023

HAL is a multi-disciplinary open access archive for the deposit and dissemination of scientific research documents, whether they are published or not. The documents may come from teaching and research institutions in France or abroad, or from public or private research centers.

L'archive ouverte pluridisciplinaire **HAL**, est destinée au dépôt et à la diffusion de documents scientifiques de niveau recherche, publiés ou non, émanant des établissements d'enseignement et de recherche français ou étrangers, des laboratoires publics ou privés.

Distributed under a Creative Commons Attribution 4.0 International License

Check for updates

Chemistry–A European Journal

Research Article
doi.org/10.1002/chem.202301780

Chemistry Europe
European Chemical Societies Publishing

www.chemeurj.org

Regime Switch in the Dual-Catalyzed Coupling of Alkyl Silicates with Aryl Bromides

Khaoula Jaouadi,[a] Mehdi Abdellaoui,[b] Etienne Levernier,[b] Pierre-Adrien Payard,[a] Etienne Derat,[b] Thomas Le Saux,[c] Cyril Ollivier,[b] Stéphane Torelli,[d] Ludovic Jullien,[c] Raphaël Plasson,*[e] Louis Fensterbank,*[b] and Laurence Grimaud*[a]

Metallaphotoredox catalyzed cross-coupling of an arylbromide (Ar–Br) with an alkyl bis(catecholato)silicate (R–Si$^{\ominus}$) has been analyzed in depth using a continuum of analytical techniques (EPR, fluorine NMR, electrochemistry, photophysics) and modeling (micro-kinetics and DFT calculations). These studies converged on the impact of four control parameters consisting in the initial concentrations of the iridium photocatalyst ($[Ir]_0$), nickel precatalyst ($[Ni]_0$) and silicate ($[R–Si^{\ominus}]_0$) as well as light intensity I_0 for an efficient reaction between Ar–Br and R–Si$^{\ominus}$. More precisely, two regimes were found to be possibly at play. The first one relies on an equimolar consumption of Ar–Br with R–Si$^{\ominus}$ smoothly leading to Ar–R, with no side-product from R–Si$^{\ominus}$ and a second one in which R–Si$^{\ominus}$ is simultaneously coupled to Ar–Br and degraded to R–H. This integrative approach could serve as a case study for the investigation of other metallaphotoredox catalysis manifolds of synthetic significance.

Introduction

Transition metal-catalyzed cross-coupling reactions occupy nowadays a prominent position in the manufacturing of drugs, agrochemicals and other important fine chemicals.[1] To a large extent, these processes have relied on the reactivity of an organometallic reactant as nucleophilic component with an electrophile (Scheme 1a), thereby suffering from several limitations such as the necessary preformation of the rather unstable organometallic partners with limited functionalization and also sometimes the recourse to undesirable reaction conditions. As an alternative, metallaphotoredox catalysis, i.e. the merger of organometallic catalysis with photocatalysis through two interconnected cycles[2] has profoundly changed the strategies for carrying out cross-coupling reactions, especially when it comes to connecting a sp^2 carbon to a sp^3 carbon. The so-called single electron transmetalation,[3] which consists in alkyl transfer through combination of a radical species originating from the photoredox catalytic cycle with a transition metal complex precludes a high activation energy for the transmetalation step (Scheme 1b). In most cases nickel-based catalysts are used in order to suppress β-hydride elimination processes. First staged with carboxylates as radical precursors by Doyle and MacMillan[4] and with trifluoroborates by Molander,[5] a series of reports have confirmed the synthetic viability of this approach, notably by featuring also other radical precursors such as sulfinates,[6] dihydropyridines,[7] Katritzky pyridium salts[8,9] cycloalkanols,[10] as well as radicals arising from direct hydrogen atom transfer (HAT).[11] Among all the possible alkyl radical precursors, bis(catecholato)silicates developed by us[12,13] and Molander[14] own the valuable property to display the lowest oxidation potentials (< 1.0 V vs SCE) ensuring the generation of a broad range of radical intermediates.

In contrast to the abundancy of versatile synthetic applications, mechanistic determinations, especially those based on thorough experimental investigations have remained scarce and not fully conclusive especially if one focuses on C–C bond formation(s). Based on the assumption of the formation of an $ArRNi^{III}X$ intermediate, which undergoes reductive elimination to produce Ar–R and $Ni^{I}X$, two pathways converging to this Ni^{III} intermediate can be envisaged. The initial proposed mechanism (variant A of the Ni cycles, Scheme 1c) was based on the known

[a] Dr. K. Jaouadi, Dr. P.-A. Payard, Dr. L. Grimaud
LBM, Département de chimie
École Normale Supérieure
PSL University, Sorbonne Université, CNRS
75005 Paris (France)
E-mail: laurence.grimaud@ens.psl.eu

[b] Dr. M. Abdellaoui, Dr. E. Levernier, Dr. E. Derat, Dr. C. Ollivier, Prof. L. Fensterbank
Sorbonne Université
CNRS, Institut Parisien de Chimie Moléculaire
75005 Paris (France)
E-mail: louis.fensterbank@sorbonne-universite.fr

[c] Dr. T. Le Saux, Prof. L. Jullien
PASTEUR, Département de chimie
École Normale Supérieure
PSL University, Sorbonne Université, CNRS
75005 Paris (France)

[d] Dr. S. Torelli
Univ. Grenoble Alpes, CNRS, CEA, IRIG
Laboratoire de Chimie et Biologie des Métaux
17 rue des Martyrs, 38054 Grenoble Cedex (France)

[e] Dr. R. Plasson
UMR408 SQPOV Avignon Université/INRAE
Campus Jean-Henri Fabre
301 rue Baruch de Spinoza BP 21239, 84916 Avignon Cedex 9 (France)
E-mail: raphael.plasson@univ-avignon.fr

Supporting information for this article is available on the WWW under https://doi.org/10.1002/chem.202301780

© 2023 Wiley-VCH GmbH

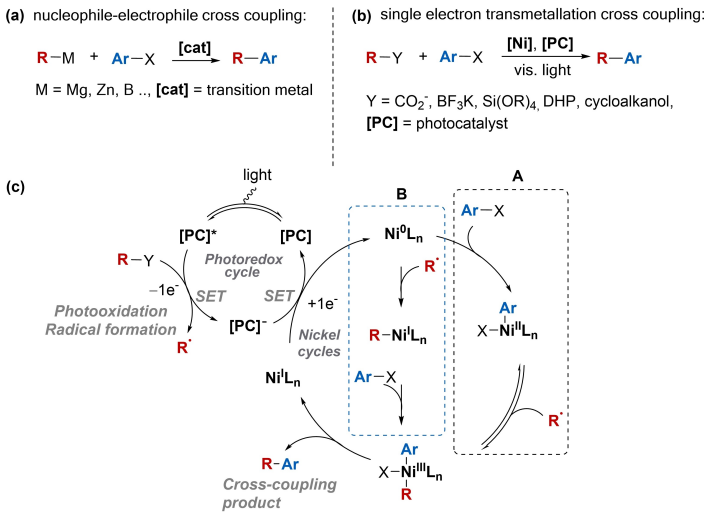

Scheme 1. Cross-coupling strategies and current mechanistic proposals for photoredox/nickel dual catalysis.

affinity of organic radicals for Ni^{II} complexes.[15,16] Thus, following oxidative addition of Ar–X onto Ni^0, the alkyl radical stemming from the photo-oxidative catalytic cycle would add to the $ArNi^{II}X$ complex to generate $ArRNi^{III}X$ that undergoes reductive elimination to deliver the Ar–R coupling product. Reduction of Ni^I by single electron transfer (SET) restores Ni^0. Interestingly, DFT calculations by Molander and Kozlowski based on benzyltrifluoroborate as radical precursor and a bipyridine-based Ni complex suggested a second possible and energetically favorable pathway consisting in the formation of a RNi^I intermediate after radical capture by Ni^0 (variant B, Scheme 1c).[17] The latter undergoes oxidative addition to yield to the same Ni^{III} complex as before. Additional calculations were reported by Molander and Gutierrez on the cross-coupling of tertiary radicals, which showed a significant ligand dependence since the anionic 2,2,6,6-tetramethyl-3,5-heptanedionate ligand outcompeted the classically used bipyridine ligands.[18] The difference in reactivity between the two ligands was attributable to the energy barriers of the reductive elimination step.[19] The authors also refined the previous calculations.[17] They confirmed the $Ni^0/Ni^I/Ni^{III}$ path to be the least energetic. A similar mechanism was also proposed for the arylation of Csp^3-H bonds promoted by decatungstate and nickel catalysis.[20]

In parallel to these theoretical advances, significant knowledge has been garnered on the photochemistry of bipyridine-ligated Ni^{II} and Ni^I complexes. Notably, $ArNi^{II}X$ complexes can undergo photo-excitation through a MLCT process under visible light irradiation. The corresponding excited state rapidly decays to a longer-lived 3*d*–*d* state with weakened bonds, which favors homolysis of the Ni^{II}–Ar bond to generate an aryl radical and a Ni^IX complex.[21] The latter exists under an equilibrium between a monomeric and a dimeric form. The dimeric form is generally unreactive while the monomeric complexes (X=Cl or Br) can undergo oxidative addition with aryl halide derivatives.[22–25] This was for instance demonstrated by generating (bipyridine)Ni^IBr complexes through electrosynthesis,[26] radiolysis[27] and submitting them to haloarenes. Moreover, a Ni^ICl complex coordinated by a diester-substituted bipyridine ($(EtO_2C)_2$bpy) ligand was studied and shown to undergo oxidative addition with arylbromides.[28] Very recently, Ben-Tal and Lloyd-Jones investigated the mechanism of a Ni/Ir-photocatalyzed reductive coupling of an aryl bromide with an alkyl bromide, featuring extensive kinetic studies. Combining mechanistic studies and microkinetic modeling, they demonstrated that the oxidative addition complex ArNiBr is an on-cycle species and they notably showed that four parameters – [ArBr], [Ni], [Ir], and light intensity – were key to control the reaction rate of ArBr whereas $[(TMS)_3SiH]$ and [RBr] control the selectivity.[29]

In this context, we went beyond these relevant findings, by developing a thorough kinetic and mechanistic study of the representative cross-coupling of an alkyl bis(catecholato)silicate with an aryl halide under dual photo/nickel catalysis conditions. This study was performed thanks to the combination of analytical techniques and modeling. The impact of each parameter on the kinetics of a model system (stoichiometry of the reactants, nature and quantities of catalysts, light intensity) was assessed and an integrative approach based on kinetic modeling was applied to propose a mechanism consistent with the collected data. Remarkably, two regimes turned out to be operative: during the first phase both substrates are consumed at the same rate but in the second regime, two $R–Si^{\ominus}$ are needed as one decomposed into R–H.

Results and Discussion

The model system

In order to study the mechanism of the cross-coupling of alkylsilicates with aryl halides under dual photo/nickel catalysis conditions, we adopted the 2-bromo-5-fluorotoluene (Ar–Br) and 3-acetoxypropyl bis(catecholato)silicate ($R–Si^{\ominus}$) as model partners, and based on our previous work,[12,13] an Ir^{III} photocatalyst and a $Ni^{II}Br_2$(dtbbpy) nickel precatalyst generated from

© 2023 Wiley-VCH GmbH

15213765, 0, Downloaded from https://chemistry-europe.onlinelibrary.wiley.com/doi/10.1002/chem.202301780 by Inrae - Dipso, Wiley Online Library on [17/10/2023]. See the Terms and Conditions (https://onlinelibrary.wiley.com/terms-and-conditions) on Wiley Online Library for rules of use; OA articles are governed by the applicable Creative Commons License

a mixture of $NiBr_2$ and 2,6-di-*tert*-butylpyridine (dtbbpy) – noted $Ni^{II}Br_2$ in the following (Scheme 2). This Ar–Br was notably selected for analytical purposes due to the presence of the fluorine atom facilitating NMR probing and the *ortho*-methyl group that could enhance the stability of the intermediate $ArNi^{II}$ complex.[30] For mechanistic analysis, we further synthesized *cis*-[(4-F-2-Me-C_6H_3)Ni^{II}Br(dtbbpy)] and [Ni^{I}Cl(dtbbpy)]$_2$, respectively denoted $ArNi^{II}$Br and Ni^{I}Cl in the following.

Investigation of the Ir-based photocatalytic cycle

As light on/off experiments showed that the photoconversion of the system stopped without irradiation,[31] thereby discarding long radical chain mechanisms,[32] we could directly apply irradiation on an NMR tube containing the photoreactive medium with a home-built setup (see Figure S1) in order to sequentially get quantitative information by $^{19}F\{^1H\}$ NMR. Indeed, as complex polymers are generated all along the process due to the release of the bis(catecholato)silane,[33] a continuous shaking ensures a homogeneous irradiation of the medium. We set the irradiation conditions upon consideration of two series of observations. First, we noticed that the Ir^{III} photocatalyst exhibits a much more important light absorption at wavelengths lower than 450 nm, which corresponds to the blue LED emitting region used for the scope investigation[12,13] (see Figure S7b). Second, the UV absorption spectrum of the $ArNi^{II}$Br reference complex proved that its absorption was less pronounced around 360 nm than around 450 nm (see Figure S7a). As previously reported,[21,34,35,36] the photodegradation of $ArNi^{II}$Br may occur above 400 nm and indeed it was faster upon illumination at 450 than at 365 nm (see Figure S9). Accordingly, we used a UV LED emitting at 365 ± 5 nm for irradiation of the selected model reaction. At 15 mW.cm^{-2} light intensity, the photoconversion of Ar–Br and R–$Si^{\ominus}$ proceeded smoothly to yield up to 80% of Ar–R along with traces of arylated by-products Ar–H and Ar–Ar, as well as R–$Si^{\ominus}$-derived side products such as R–H and traces of R–R. It is worth noting that no continuous consumption of R–$Si^{\ominus}$ was evidenced when irradiating it with the photocatalyst only, which implies a direct link between the photoconversion and the presence of Ni catalyst.

Through the control of all the parameters, the light-driven generation of radicals from silicates could be studied. Alkyl bis(catecholato)silicates have been reported to quench the excited state Ir^{III}* of the photocatalyst, with a high rate constant ($\approx 10^{10}$ M^{-1} s^{-1}) assessed from Stern–Volmer analysis of the dependence of the Ir^{III}* steady luminescence on the concentration of bis(catecholato)alkylsilicates.[12] The order of magnitude of this value was presently confirmed by using the Stern–Volmer analysis of the dependence of the Ir^{III}* luminescence lifetime on the R–$Si^{\ominus}$ concentration (see Figure 1a,b). Since the Ir^{III}* luminescence emission spectrum does not overlap with the R–$Si^{\ominus}$ absorption spectrum (see Figure S8), energy transfer[37,38] is unlikely and the photogeneration of radicals from R–$Si^{\ominus}$ probably results from electron transfer. This conclusion is consistent with electrochemical considerations. Ir^{III}* (reduction potential $E_p^{red} = +1.32$ V vs SCE[39] in DMF) is anticipated to oxidize R–$Si^{\ominus}$ ($E_{p/2}^{ox} = +0.85$ V vs SCE in DMF; see Figure S12g). In contrast, *fac*-Ir(ppy)$_3$ featuring photophysical properties close to those of Ir^{III} but exhibiting a lower reduction potential at the excited state than Ir^{III}* ($E_p^{red} = +0.31$ V vs SCE)[40] does not lead to photoconversion when irradiated at 365 nm (see Table S1). Another argument was provided by EPR experiments performed in DMF. As expected, Ir^{III} and the 1/1 mixture of Ir^{III}/R–$Si^{\ominus}$ are EPR-silent without irradiation either in frozen solution (180 K) or at room temperature (298 K). In contrast, after 2 min irradiation, Ir^{III} remains EPR-inactive (Figure 1c) but the Ir^{III}/R–$Si^{\ominus}$ mixture exhibits an axial EPR signal at 180 K with $g_{iso} = 1.98$ ($g_1 = g_2 = 1.99$ and $g_3 = 1.95$, Figure 1d), which shows that the R–$Si^{\ominus}$ presence is crucial to photo-generate a reduced Ir^{II} species. The g_{iso} value, very close to g_e (free electron), suggests the presence of an organic radical in the mixture. This observation is consistent with the accumulation of one electron spin density on the bipyridine, which is also deduced from analysing by DFT (at the ωB97M-D3BJ/def2-SV(P) level) (Figure 1e) the atomic spin densities of the radical anion of the reduced complex Ir[dF(CF_3)ppy)$_2$(bpy)$^{-\bullet}$] (abbreviated Ir^{II} as generally written). To ascertain the g_{iso} value, we resorted to complete active space self-consistent field (CASSCF) calculations on the reduced Ir^{II} species as already described in the literature for similar complexes.[41] Namely, all the key *d* orbitals on the metal center and the π-system of the bpy were included (13 electrons in 13 orbitals) on the C2 symmetric complex.[42] We calculated a

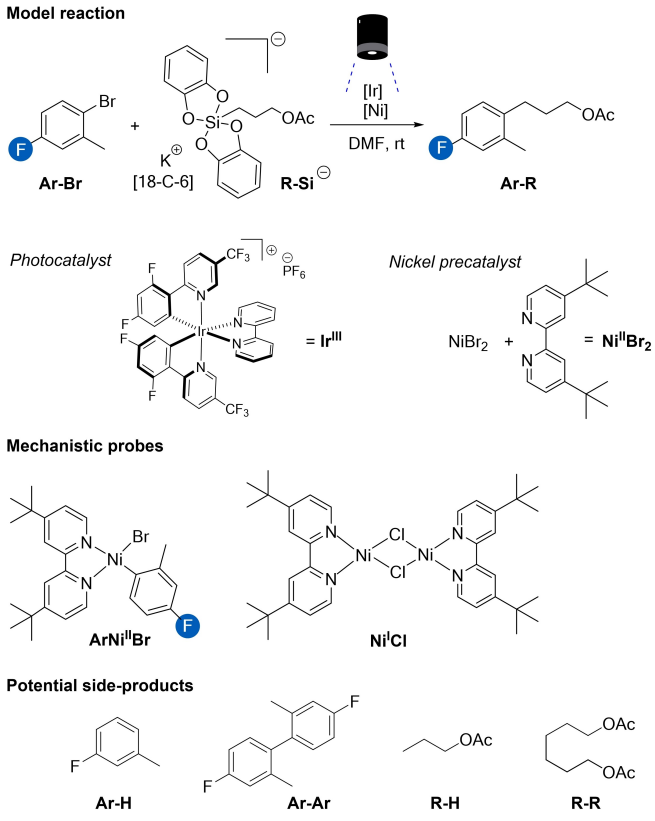

Scheme 2. Model system, possible intermediates and by-products.

© 2023 Wiley-VCH GmbH

15213765, 0, Downloaded from https://chemistry-europe.onlinelibrary.wiley.com/doi/10.1002/chem.202301780 by Inrae - Dipso, Wiley Online Library on [17/10/2023]. See the Terms and Conditions (https://onlinelibrary.wiley.com/terms-and-conditions) on Wiley Online Library for rules of use; OA articles are governed by the applicable Creative Commons License

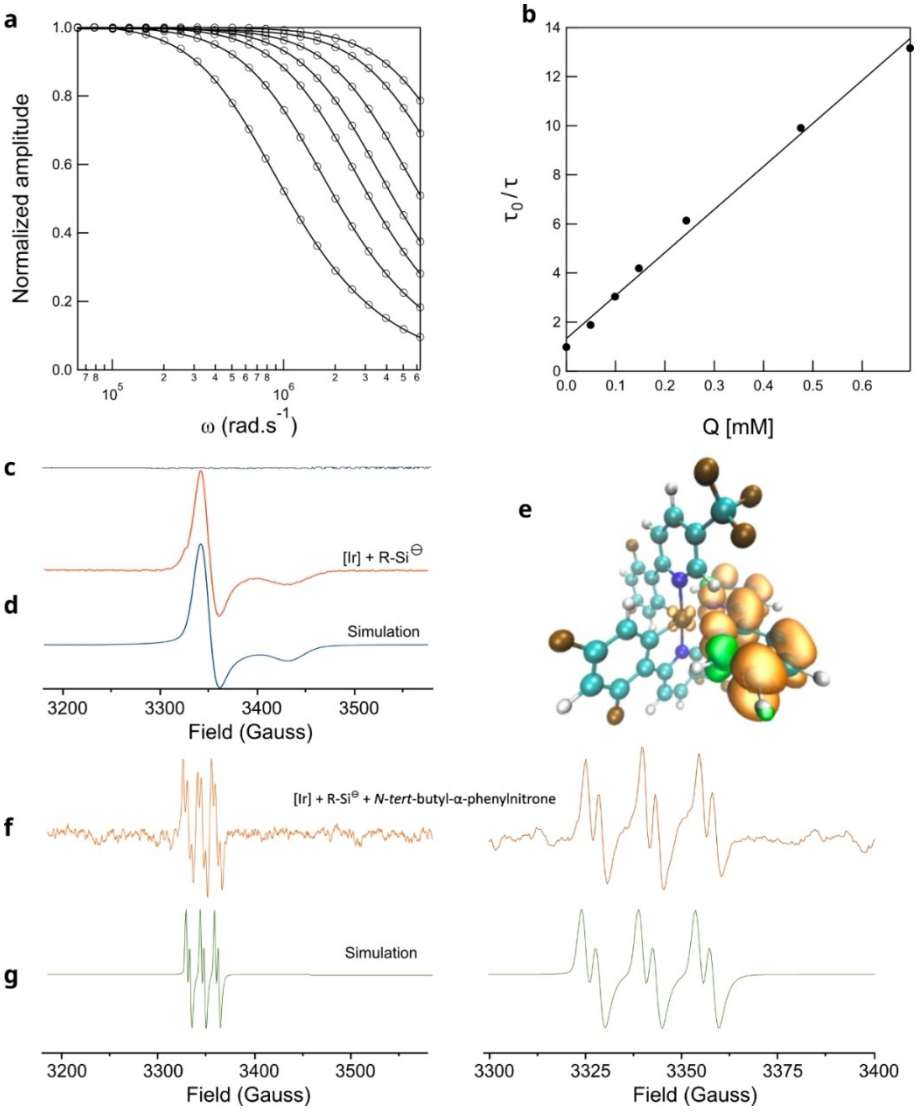

Figure 1. Investigation of the Ir-based photocatalytic cycle. (a,b): Dependence of the normalized amplitude of the luminescence response of 5 μM Ir^{III} on the angular frequency ω of the light modulation (a) and associated Stern–Volmer analysis (b; slope = 17.5 ± 0.6 mM^{-1}, $r^2 = 0.993$) at various concentrations (mM) of R–$Si^{\ominus}$ (0, 0.05, 0.1, 0.15, 0.25, 0.5 yielding the following lifetimes τ(μs): 1.6, 0.9, 0.5, 0.4, 0.3, 0.2). Solvent: DMF; temperature: 298 K; (c,d): X-band (9.43 GHz) EPR spectra in DMF at 180 K after 2 min irradiation at 450 nm of Ir^{III} at 2.5 mM (c) and 2.5 mM Ir^{III}/R–$Si^{\ominus}$ 1/1 mol/mol mixture with the corresponding simulation using $g_1 = 2.000$; $g_2 = 1.999$; $g_3 = 1.949$, $g_{iso} = 1.983$ (d); (e): Atomic spin densities of the reduced complex $Ir[dF(CF_3)ppy)_2(bpy)^{-\bullet}]$ radical anion; (f,g): X-band (9.43 GHz) EPR spectra of 2.5 mM Ir^{III}/R–$Si^{\ominus}$ 1/1 mol/mol mixture in the presence of an equimolar amount of *N-tert*-butyl-α-phenylnitrone at 298 K after 5 min irradiation at 450 nm (f) and the corresponding simulation using a_N 14.8 MHz, a_H 3.5 MHz = and g_{iso} = 2.0056 (g). Microwave parameters: 0.02 mW (at 180 K) and 20 mW (at 298 K), 5 scans, Mod. Ampl. 2G, Mod. Freq. 100 kHz, Time Const. 81.92 s, Conv. Time 20.48 s, $B_1 \perp B$.

$g_{iso} = 1.979$ ($g_1 = 1.988$, $g_2 = 1.987$ and $g_3 = 1.963$) that is in good agreement with experimental values (Figure 1d).

The evidence for the production of radicals from illumination of the Ir^{III}/R–$Si^{\ominus}$ mixture was eventually provided by spin trap experiments. After 5 min of irradiation in the presence of an equimolar amount of *N-tert*-butyl-α-phenylnitrone,[43] a new EPR signal consisting in a triplet of doublet was observed at room temperature (Figure 1f). This signal could be best simulated considering hyperfine couplings of the unpaired electron with one nitrogen (^{14}N, I = 1) and one hydrogen (^{1}H, I = $^{1}/_{2}$) with $g_{iso} = 2.0056$; $a_N = 14.8$ MHz and $a_H = 3.5$ MHz (Figure 1g). This observation is in line with the formation of the carbon-based adduct resulting from the trapping of the $R^{\bullet}$ radical generated from R–$Si^{\ominus}$ upon irradiation.

Thus, consistent with the mechanism generally proposed for its action as photocatalyst, Ir^{III} is activated by photon absorption to Ir^{III}*, that in turns can relax back to Ir^{III}, or react by SET with R–$Si^{\ominus}$ leading to the formation of Ir^{II} and the alkyl radical $R^{\bullet}$. The rate constants of the two latter reactions are much higher than the one associated with the process of light absorption. Hence the steady concentration of Ir^{III}* is vanishing compared to the Ir initial concentration, which thus essentially rests in both Ir^{II} and Ir^{III} forms.

© 2023 Wiley-VCH GmbH

15213765, 0, Downloaded from https://chemistry-europe.onlinelibrary.wiley.com/doi/10.1002/chem.202301780 by Inrae - Dipso, Wiley Online Library on [17/10/2023]. See the Terms and Conditions (https://onlinelibrary.wiley.com/terms-and-conditions) on Wiley Online Library for rules of use; OA articles are governed by the applicable Creative Commons License

Investigation of the Ni-based catalytic cycle

In contrast to the absence of continuous consumption of R–Si$^{\ominus}$ upon illumination in the presence of the photocatalyst only, adding the Ni catalyst enables us to regenerate Ir^{III} from Ir^{II} and get continuous consumption of R–Si$^{\ominus}$ and Ar–Br.

To decipher the Ni-based catalytic cycle, we first performed a large series of kinetic experiments. The reactive system was exposed to irradiation and $^{19}F\{^{1}H\}$ NMR was used to analyze the time evolution of the concentrations of Ar–Br reactant and Ar–R product upon varying the control parameters (total concentration $[Ni]_0$ and $[Ir]_0$ in Ni and Ir catalysts, light intensity I_0, stoichiometry of the reactants; see Table S2). Figure 2a displays a representative time evolution of the concentrations [Ar–Br] and [Ar–R] with initial concentrations $[R–Si]_0 = 0.15$ M, $[Ar–Br]_0 = 0.1$ M, $[NiBr_2]_0 = 6$ mM, $[Ir]_0 = 2$ mM, and light intensity at 365 nm $I_0 = 15$ mW.cm^{-2}. The whole set of time evolutions is given in Figure S18.

Under all the experimental conditions explored in this study, we observed the drop of the Ar–Br concentration associated

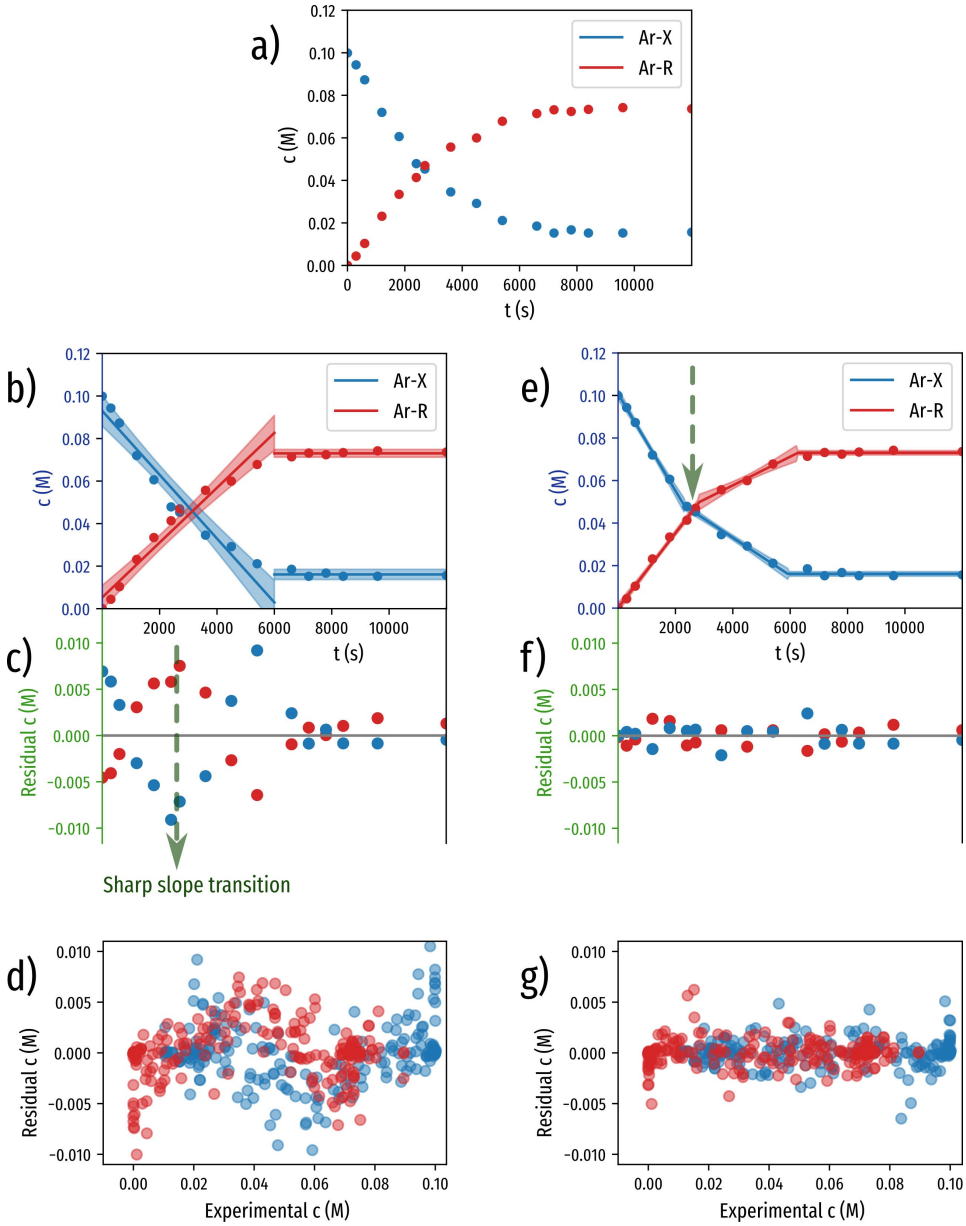

Figure 2. Processing of the kinetic experiments on the Ni-based catalytic cycle. Investigation of the Ni-based catalytic cycle. (a): Time evolution of the concentrations of Ar–Br reactant and the Ar–R product. Experimental conditions: $[R–Si^{\ominus}]_0 = 0.15$ M, $[Ar–Br]_0 = 0.1$ M, $[Ni^{II}Br_2]_0 = 6$ mM, $[Ir]_0 = 2$ mM, $I_0 = 15$ mW.cm^{-2}; (b): Linear fit of the data displayed in (a) over the kinetic window [0; t_{end}] of time variation of the concentrations of Ar–Br and Ar–R;); (c) Residuals of the concentrations in Ar–Br and Ar–R extracted from applying the linear fit displayed in (b); (d) Overlap of the residuals of the concentrations in Ar–Br and Ar–R extracted from applying the linear fit on all the kinetic experiments reported in Table S2 and Figure S18; (e): Bilinear fit of the data displayed in (a) over the kinetic window [0;t_{switch}] and [t_{switch}; t_{end}] of time variation of the concentrations of Ar–Br and Ar–R;); (f) Residuals of the concentrations in Ar–Br and Ar–R extracted from applying the bilinear fit displayed in (e); (g) Overlap of the residuals of the concentrations in Ar–Br and Ar–R extracted from applying the bilinear fit on all the kinetic experiments reported in Table S2 and Figure S18.

© 2023 Wiley-VCH GmbH

15213765, 0, Downloaded from https://chemistry-europe.onlinelibrary.wiley.com/doi/10.1002/chem.202301780 by Inrae - Dipso, Wiley Online Library on [17/10/2023]. See the Terms and Conditions (https://onlinelibrary.wiley.com/terms-and-conditions) on Wiley Online Library for rules of use; OA articles are governed by the applicable Creative Commons License

with a symmetrical rise of the Ar–R one followed by a final phase of saturation starting at time t_{end}. Moreover, depending on the experimental conditions, we further noticed a linear evolution of the concentration profiles of Ar–Br and Ar–R (e.g. see entries 3 and 14 of Figure S18). This behavior suggested a zeroth order kinetics in R–Si$^{\ominus}$ and Ar–Br reactants, which could further be in line with the kinetic behavior expected from the photocatalytic system displayed in Scheme 1 (see subsection 7.2 of the Supporting Information).

Hence, we first applied a linear fitting function over the time window of the variation of the concentrations in Ar–Br and Ar–R shown in Figure 2a. Figure 2b and c display the resulting processing of the data together with the fitting residuals respectively. Whereas the linear fitting function could be acceptable at first sight, the residuals exhibit deviations, which are not compatible with validating the relevance of the linear fit. More precisely, they show systematic deviations, which suggest the succession of two kinetic regimes of linear variation of the concentrations of Ar–Br and Ar–R. This trend was further strengthened when examining the residuals obtained from linear fit of the whole set of experiments displayed in Figure S18 (Figure 2d). As a general behavior, the deviations are positive at short times, vanish at an intermediate time (subsequently denoted t_{switch}), and then become negative. This observation has suggested that the concentrations of Ar–Br and Ar–R linearly evolve with a higher rate in a first kinetic regime and then experience a transition towards a second kinetic regime of linear variation of the concentrations of Ar–Br and Ar–R at a slower rate. Interestingly, the slope breaking of the residual observed at the shortest time scale provides an objective criterion to define the time t_{switch} at which the transition of kinetic regime occurs.

Therefore we implemented a two-step linear fitting protocol to account for the observed kinetic behavior over the [0; t_{switch}] and [t_{switch}; t_{end}] time windows. Figure 2e and f display the result of this new data processing together with the fitting residuals respectively. The residuals are now symmetrically distributed over the whole range of concentrations, which is expected from a satisfactory fit. Figure 2g shows that this trend is general for the whole set of kinetic experiments.

Applying the bilinear fitting function to all our kinetic data revealed several features:

- A short induction phase for experiments performed with a $Ni^{II}Br_2$ as pre-catalyst (lasting *ca.* 10 min, when complete transformations are performed at a timescale of *c. a.* 10^3 min) associated with much slower consumption and production of Ar–Br and Ar–R respectively (see Figure 3a);
- A first phase of linear consumption of Ar–Br and production of Ar–R. It initially occurs at a constant rate φ_1 and it switches at time t_{switch} towards a second phase of linear consumption of Ar–Br and production of Ar–R with an associated rate φ_2, corresponding to about half the rate φ_1 of the first phase (see Figure 2e and Table S2).
- A final phase of saturation of consumption of Ar–Br at a time t_{end}, before the full consumption of Ar–Br, which produces Ar–R in 70%–80% yield in the presence of 1.5 equiv. of R–Si$^{\ominus}$ (see Figure 2a). Figure 3b shows that the normalized time evolutions of the concentration of Ar–Br are similar when using different amounts of R–Si$^{\ominus}$ under the same experimental conditions. However, the photoconversions at low initial R–Si$^{\ominus}$ concentrations exhibit low yield and early t_{end}, while excess of R–Si$^{\ominus}$ is necessary for the full conversion of Ar–Br at high t_{end}. Interestingly, adding further R–Si$^{\ominus}$ after t_{end} enables the reaction to start again at the same initial rate, eventually yielding the consumption of the remaining Ar–Br (see Figure S17). In particular, this observation discards any explanation of the kinetic behavior that would originate from inhibition of the reaction rate by a product of the photoconversion;
- Finally, all the experiments yield the same value of the product $\varphi_1 \times t_{end}$ (0.11 ± 0.1 M, see Table S2 and Figure S18). This kinetic behavior is consistent with a first phase where both Ar–Br and R–Si$^{\ominus}$ are consumed at the same rate φ_1, and a second phase where Ar–Br is consumed at the halved rate φ_2 while R–Si$^{\ominus}$ keeps being consumed at rate φ_1.

Then we performed complementary experiments to identify productive intermediates in the Ni-based catalytic cycle and estimate their rate constants.

We first changed the source of nickel to generate the catalyst and noticed that the induction phase disappears by using either $Ni(COD)_2$ with one equivalent of the dtbbpy ligand, $Ni^{I}Cl$, or $ArNi^{II}Br$ instead of $Ni^{II}Br_2$ (see Figure 3a and Supporting Information, Section 6.2). These observations led us to conclude that the induction phase originates from the reduction of $Ni^{II}Br_2$ to form the active catalyst as with other pre-catalysts the formation of Ar–R started with no delay. Moreover, the thermodynamically favored reduction of $Ni^{I}X$ complex ($E_p^{red} \approx -1.2$ V vs SCE in DMF) by the Ir^{II} species to regenerate Ni^0 is consistent with Ni^{I} to be a competent intermediate in the Ni-based catalytic cycle.[44]

We then investigated the oxidative addition of Ar–Br to Ni^0 by performing cyclic voltammetry toward reduction potentials at various scan rates in the presence of a large excess of Ar–Br.[45] $Ni^{II}Br_2$ first undergoes two-electron reduction at R_1 to yield Ni^0. Ni^0 is subsequently either back oxidized at O_1 or trapped in situ by oxidative addition to generate $ArNi^{II}Br$ (Figure 3c), which has been characterized by its second reduction peak at R_2 from comparison with the voltammogram of a $ArNi^{II}Br$ sample (Figure 3d). Quantified from the drop of the oxidation wave O_1 (Figure 3c), the proportion of trapped Ni^0 increases when the scan rate is decreased (see Figure S15).[46] Data processing enabled us to retrieve 25 $L.mol^{-1}.s^{-1}$ for the value of the bimolecular rate constant associated with the oxidative addition of Ar–Br to Ni^0(dtbbpy) at 293 K,[47] which is consistent with the one determined for the analogous Ni^0(bpy) complex with Ph–Br.[48]

We eventually analyzed the reactivity of $ArNi^{II}Br$. This complex does not react with R–Si$^{\ominus}$ upon irradiating at 365 nm in the absence of Ir^{III}. However, it traps a primary radical generated from heating dilauryl peroxide and the resulting Ni^{III} complex rapidly evolves to yield the cross-coupling product (Figure 3e) as evidenced by the characteristic signal at -119.5 ppm by $^{19}F\{^1H\}$ NMR and further confirmed by mass spectrometry (see Supporting Information, section 6.5, Figures S15).[16,49] Hence, the observed intermediates of the Ni-based mechanism as well as their reactivity are consistent with the variant A of the Ni cycle of Scheme 1c.

© 2023 Wiley-VCH GmbH

15213765, 0, Downloaded from https://chemistry-europe.onlinelibrary.wiley.com/doi/10.1002/chem.202301780 by Inrae - Dipso, Wiley Online Library on [17/10/2023]. See the Terms and Conditions (https://onlinelibrary.wiley.com/terms-and-conditions) on Wiley Online Library for rules of use; OA articles are governed by the applicable Creative Commons License

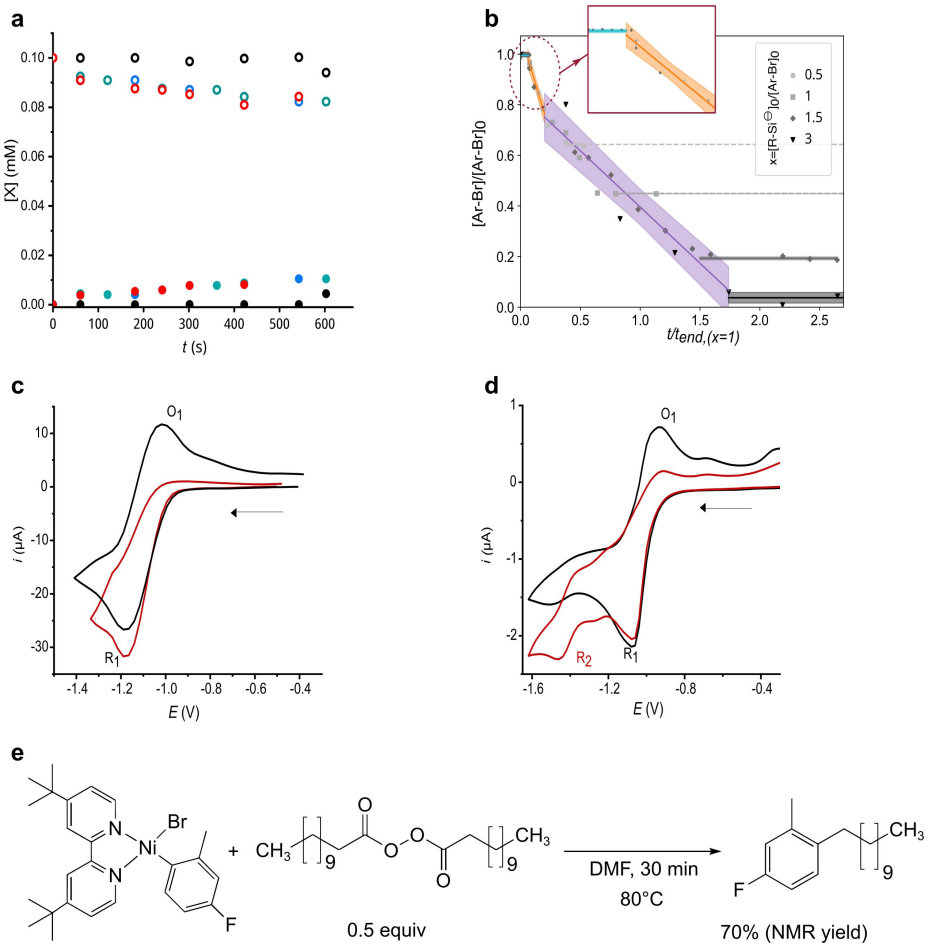

Figure 3. Investigation of the Ni-based catalytic cycle. (a): Initial time evolution of the concentrations in Ar–Br (circles) and Ar–R (disks) in reactive mixtures irradiated at 365 nm in the presence of various nickel pre-catalysts. System composition: Ar–Br (0.1 M in DMF), R–$Si^{\ominus}$ (1.5 equiv), Ir^{III} (2 mol%) with 4 mol% of $Ni^{II}Br_2$ (black) $Ni(COD)_2$/dtbbpy (blue), $ArNi^{II}Br$ (green), and $Ni^{I}Cl$ (red);); (b): Normalized time evolutions of [Ar–Br] using different amounts of silicates (experimental conditions: $[Ar–Br]_0 = 0.1$ M, $[Ni]_0 = 2$ mM, $[Ir]_0 = 4$ mM, $I_0 = 15$ mW.cm^{-2}). t_{switch} and t_{end} respectively designate the time at which the rates of consumption of Ar–Br and production of Ar–R switches from φ_1 to φ_2 and the time of the total R–$Si^{\ominus}$ consumption and of saturation of consumption of Ar–Br; (c,d): Cyclic voltammograms of 2 mM $Ni^{II}Br_2$ performed toward the reduction potentials at a steady glassy carbon (GC) disk electrode ($\phi = 3$ mm, for d at 0.1 V.s^{-1}) and for e at 0.05 V.s^{-1}) in DMF containing 0.3 M n-Bu_4NBF_4 before (black) and after (red) addition of Ar–Br (10 equiv); (e): Reaction of 25 mM $ArNi^{II}Br$ and lauroyl peroxide (0.5 equiv) after 30 min of heating at 80 °C in DMF.

However, whereas the latter mechanism correctly accounts for the 1:1 stoichiometry of the consumption of both reactants and the production of the Ar–R product in an initial kinetic regime, it is not in line with the 2:1 stoichiometry observed at longer timescales nor on the observed additional R–H production.

Step by step kinetic modeling

The latter discrepancy led us to propose an expanded mechanism, which has been built by a stepwise process. Starting from a minimal model involving a few reactions, we incrementally added more reactions in order to account for the succession of experimentally observed kinetic regimes. At each step of kinetic modeling, we considered the steady-state to be reached. Hence, we could lead an analytic calculation of the fluxes of reactions within the catalytic cycles upon assuming the nature of their resting states. These analytic developments, linked to experimental kinetic data, could lead to the evaluation of missing kinetic parameters. The details are provided in Section 7 of the Supporting Information and the main results are reported below.

Qualitatively, the kinetic behavior can be explained by the occurrence of two different mechanisms in each kinetic regime: the originally expected mechanism in the first regime (with an overall conversion R–$Si^{\ominus}$ + Ar–Br → Ar–R + $Br^{\ominus}$ + Si), and a second mechanism in the second kinetic regime where R–$Si^{\ominus}$ is simultaneously coupled to Ar–Br and degraded (i.e. 2R–$Si^{\ominus}$ + Ar–Br + H^+ → Ar–R + $Br^{\ominus}$ + 2Si + R–H). As a consequence, whereas Ar–Br and Ar–R are consumed and produced at distinct rates φ_1 and φ_2 with $\varphi_1 \approx 2\varphi_2$ before and after t_{switch} respectively, R – $Si^{\ominus}$ is converted at a constant rate, φ_1 until t_{swich} then $2\varphi_2$ until t_{end}.

We first addressed the iridium catalytic cycle. In the first stage model, this photocycle drives the reduction of a generic oxidant Ox (Figure 4a). This simple model satisfactorily yields a zeroth order kinetics in R–$Si^{\ominus}$.

© 2023 Wiley-VCH GmbH

15213765, 0, Downloaded from https://chemistry-europe.onlinelibrary.wiley.com/doi/10.1002/chem.202301780 by Inrae - Dipso, Wiley Online Library on [17/10/2023]. See the Terms and Conditions (https://onlinelibrary.wiley.com/terms-and-conditions) on Wiley Online Library for rules of use; OA articles are governed by the applicable Creative Commons License

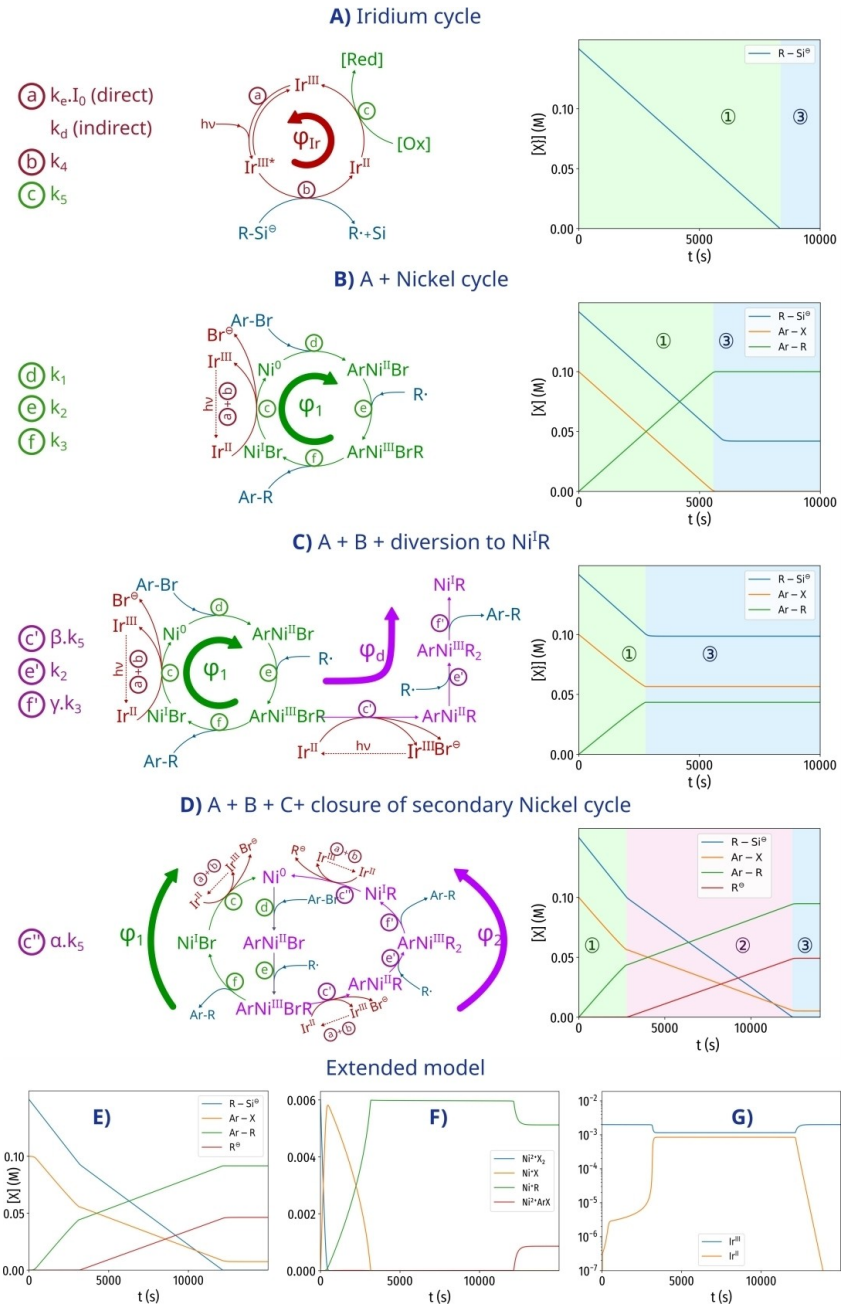

Figure 4. Step-by-step modeling of the Ir/Ni catalytic cycles. A) Iridium cycle. Under continuous recycling of Ir^{III} from Ir^{II} by reaction with an oxidant (phase ①), the irradiation of Ir^{III} governs the continuous reaction of R–$Si^{\ominus}$ at a constant rate φ. The light-driven conversion stops when there is no more R–$Si^{\ominus}$ left (phase ③). B) Upon coupling to a first Ni cycle, the Ir cycle drives the equimolar consumption of R–$Si^{\ominus}$ and Ar–Br, and formation of Ar–R at a constant rate φ_1 (phase ①). When R–$Si^{\ominus}$ is in excess, the light-driven conversion stops when there is no more Ar–Br left (phase ③). C) The addition of a slow diverting path leading to the accumulation of $Ni^{I}R$ at a rate φ_d shortens the phase of equimolar consumption of R–$Si^{\ominus}$ and Ar–Br, and formation of Ar–R (phase ①). The light-driven conversion stops before the overall consumption of both R–$Si^{\ominus}$ and Ar–Br (phase ③). D) The closure of the latter diverting path back to Ni^{0} generates a secondary Ni cycle. It results in a light-driven conversion, which occurs in two phases. After a first phase (phase ①) in which the coupling between the Ir cycle with the first Ni cycle drives the equimolar consumption of R–$Si^{\ominus}$ and Ar–Br and formation of Ar–R at a constant rate φ_1, the light-driven conversion encounters a mechanistic shift. In the second phase (phase 2), the Ir cycle is coupled with the second Ni cycle and the formation of Ar–R is accompanied by the formation of $R^{\ominus}$ at a same slower rate φ_2. In the presence of 1.5 equivalent of R–$Si^{\ominus}$ with respect to Ar–Br, the light-driven conversion stops when there is no more R–$Si^{\ominus}$ left. The simulations were performed with $k_e = 0.035\ s^{-1}$, $k_d = 4 \cdot 10^5\ s^{-1}$, $k_4 = 2.7 \cdot 10^{10}\ M^{-1}.s^{-1}$, $k_1 = 25\ M^{-1}.s^{-1}$ (constants extracted from kinetic measurements), $\lambda = 0.015$, $k_3 = 1\ s^{-1}$, $k_5 = 10^3\ M^{-1}.s^{-1}$, $\beta = 30$, $\gamma = 1$, $\alpha = 10^{-3}$ (constant estimated from the step-by-step model study, see text), and k_2 was supposed very fast, the corresponding reactions being implicitly taken into account (see Sections S7 and S8). Initial conditions were $[Ir^{III}]_0 = 2 \cdot 10^{-3}$ M, $[R\text{–}Si^{\ominus}]_0 = 0.15$ M in A–D, $[Ox]_0 = 0.5$ M in A, $[Ni^{I}\text{-}X]_0 = 6 \cdot 10^{-3}$ M and $[Ar\text{–}Br]_0 = 0.1$ M in B–D.E–G) Extended kinetic model taking explicitly into account all the reactions of D), with the addition of the reduction of $NiBr_2$ by Ir(II). E: Time evolution of the major reactants; F: Time evolution of the major nickel complexes; G: Time evolution of the major iridium complexes (for more details, see Figure S20b).

© 2023 Wiley-VCH GmbH

15213765, 0, Downloaded from https://chemistry-europe.onlinelibrary.wiley.com/doi/10.1002/chem.202301780 by Inrae - Dipso, Wiley Online Library on [17/10/2023]. See the Terms and Conditions (https://onlinelibrary.wiley.com/terms-and-conditions) on Wiley Online Library for rules of use; OA articles are governed by the applicable Creative Commons License

The iridium catalytic photocycle was then connected to a first nickel-based catalytic cycle, in place of the generic Ox/Red compounds (Figure 4b). At that point, it is important to note that variants A and B shown in Scheme 1c cannot be kinetically distinguished upon assuming the addition of R$^{\bullet}$ to Ni^{0} and ArNi^{II}Br to be much faster than the oxidative addition of Ar–Br. In fact, both paths can be reduced to a same mechanism by applying the steady-state approximation. In Figure 4b, we adopt the path A.

Both the iridium and the nickel cycles are strongly coupled. Each turnover of the Ir-photocycle produces one R$^{\bullet}$ and one Ir^{II}, which relaxes back to Ir^{III} by transferring one electron to the Ni cycle. Each turnover of the latter consumes one R$^{\bullet}$ and one Ni^{I}Br is reduced to Ni^{0} by accepting one electron from the Ir cycle. As a consequence, when the system reaches a steady-state production of Ar–R, both cycles are processed with the same steady rate, globally leading to the R–Si$^{\ominus}$ + Ar–Br → Si + Br$^{\ominus}$ + Ar–R conversion at the same rate φ_1 given in Equation (1) (see Supporting Information, Section 7.2 for details).

$$\varphi_1 = \frac{k_e \cdot I_0 \cdot k_5 \cdot [Ni]_0 \cdot [Ir]_0}{k_e \cdot I_0 + k_5 \cdot [Ni]_0} \quad (1)$$

As a preliminary conclusion, the kinetic model proposed in Scheme 1c satisfactorily accounts for a linear production of Ar–R by exploiting the experimentally determined rate constants. However, this kinetic model fails to describe the halving of the production rate characterized by a second slope φ_2, and the excess of R–Si$^{\ominus}$ required to reach completion for Ar–Br. As a consequence, the reported mechanism seems to correctly describe an initial phase, but another mechanism is observed at longer timescale, characterized by a slower Ar–R production at a rate φ_2, while R–Si$^{\ominus}$ keeps being consumed at about the initial rate φ_1.

As mentioned above, Ir^{II} can reduce Ni^{I}Br into Ni^{0}. Hence, one reasonably expects that other halogenated Ni complexes, such as ArNi^{III}BrR, can as well be reduced by Ir^{II}, *i.e.* leading to the formation of ArNi^{II}R with elimination of Br$^{\ominus}$. The latter complex may then in turn trap an additional radical R$^{\bullet}$, up to the formation of ArNi^{III}R$_2$. Provided that this last complex releases Ar–R (see DFT calculations below), it would yield Ni^{I}R, that is anticipated to be less easy to reduce than Ni^{I}Br by Ir^{II}. Then, Ni^{I}R would accumulate (see Figure 4c), which will depopulate the initial productive Ni-based catalytic cycle as a function of time. Considering the concentrations of ArNi^{II}Br and ArNi^{III}BrR to be low relatively to the concentration of Ni^{I}Br, the leakage flux φ_d evaluating the production of Ni^{I}R can be computed by Equation (2)

$$\varphi_d = \frac{\beta \cdot k_5^2 \cdot k_e^2}{k_3} \cdot \frac{I_o^2 \cdot [Ir]_0^2}{(k_e I_0 + k_5 \cdot [Ni^I Br])^2} \cdot [Ni^I Br] \quad (2)$$

that is slow compared to the reaction flux within the primary Ni catalytic cycle. Interestingly, when $k_5 [Ni^I Br] \gg k_e I_0$, Ni^{I}Br intervenes in this leakage flux with a kinetic order -1. As a consequence, the leakage flux *increases* on time and the overall conversion of Ni^{I}Br into Ni^{I}R is completed after the finite time t_{switch} at which the photoconversion flux switches from the primary to the secondary cycle. Indeed, the numerical simulations show that the initial productive Ni-based catalytic cycle is active at constant rate until its nearly depletion by the accumulation of Ni^{I}R (see Figure S20a). Then, the first nickel catalytic cycle abruptly stops with the depletion of Ni^{I}Br. The emergence of the corresponding switch depends on the values of the control parameters, which drive the relative values of t_{switch} and t_{end} (see Equations (14,27) in the Supporting Information). In particular, when $t_{switch} < t_{end}$, the switch occurs before the total consumption of both R–Si$^{\ominus}$ and Ar–Br.

As an additional outcome of the depletion of the primary Ni-based catalytic cycle, Ir^{II} accumulates since there is no more easily reducible Ni^{I}Br for recycling back Ir^{II} to Ir^{III}. As a consequence, less reducible species such as Ni^{I}R may in turn be reduced by Ir^{II} to Ni^{0}. It results in the activation of a secondary Ni-based catalytic cycle consuming two R$^{\bullet}$ and one Ar–Br, releasing one Ar–R with one R$^{\ominus}$ carbanion subsequently yielding R–H after protonation (see Figure 4d). This process resulted in a higher consumption of R–Si$^{\ominus}$ compared to Ar–Br. In this second kinetic regime, the overall kinetics is still governed by the reaction flux of the Ir-based catalytic cycle, but only half of the R–Si$^{\ominus}$ is converted to Ar–R, explaining the halving of Ar–R formation. In these conditions, the flux φ_2 is established within the secondary Ni-based catalytic cycle [Equation (3)]

$$\varphi_2 = \frac{\alpha \cdot k_e \cdot I_0 \cdot k_5 \cdot [Ni]_0 \cdot [Ir]_0}{k_e \cdot I_0 + 2 \cdot \alpha \cdot k_5 \cdot [Ni]_0} \quad (3)$$

where $\alpha \ll 1$, so that the secondary cycle is only efficient after the disappearance of the primary cycle.

On the basis of these analytical derivations that led to retrieve orders of magnitude of the missing kinetic parameters (see Figures S20), a numerical kinetic simulation could be set up in order to refine the values of the kinetic parameters and reproduce the observed experimental behavior (see Supporting Information, Section 8). It first confirmed the insight provided by the analytic derivations that the effective light intensity I_0 had to be decreased down to 0.015 times the value of the incident light intensity I_0^{theo}, which was independently measured (see Supporting Information, Subsection 3.1). This drop probably originates from three factors: (i) the decay of light intensity along the optical path at high absorbance; (ii) the formation of precipitates,[31] which occurs during the transformation and further decreases the penetration of light in the medium; (iii) the quenching of the excited state of Ir^{III} by other species than R–Si$^{\ominus}$ (e.g. Br^{-}), which has been evidenced by lifetime measurements (see Supporting Information, Subsection 3.4). Hence, the kinetic model globally reproduces and explains most prominent experimentally observed features (see Figure 4 E–G and Figures S20).

Validation by DFT calculations

To strengthen the conclusions of the kinetic analysis, calculations at the Density Functional Theory level were performed (see Figure 5 and Supporting Information for computational details). As reported by Molander and Kozlowski,[17] the ArNi^{II}Br complex traps the radical R$^{\bullet}$ generated from R–Si$^{\ominus}$ after SET with a low activation barrier, yielding ArNi^{III}BrR. The latter intermediate undergoes a reductive

© 2023 Wiley-VCH GmbH

15213765, 0, Downloaded from https://chemistry-europe.onlinelibrary.wiley.com/doi/10.1002/chem.202301780 by Inrae - Dipso, Wiley Online Library on [17/10/2023]. See the Terms and Conditions (https://onlinelibrary.wiley.com/terms-and-conditions) on Wiley Online Library for rules of use; OA articles are governed by the applicable Creative Commons License

elimination, which is concerted, as illustrated by the similar lengths of the broken and created bonds with a barrier similar to the SET reaction. The formation of Ar–R further liberating $Ni^{I}Br$ for a new catalytic cycle is highly exothermic (see Supporting Information, Section 10).

Considering the mechanistic path proposed for the second regime, the competition between the nickel-catalyzed formations of a Csp^2-Csp^3 or Csp^3-Csp^3 bond in $ArNi^{III}R_2$ was then examined (Figure 4). The *trans*-complex **I.1'** where the two alkyl chains are in *trans* configuration can evolve to intermediate **I.2'** where the two alkyl chains are in *cis* configuration. The latter is of similar stability than **I.1'** (ca. 0.2 kcal.mol^{-1}) and the barrier between **I.1'** and **I.2'** raises to 13.1 kcal.mol^{-1}. From **I.2'**, the reductive elimination to generate the homocoupling product proceeds with a barrier of 24.6 kcal.mol^{-1}. From **I.1'**, the reductive elimination between the alkyl chain and the aromatic moiety requires a barrier energy of 18.0 kcal.mol^{-1}. These calculations suggest that the main product of reductive elimination from $ArNi^{III}R_2$ should be the Csp^2-Csp^3 Ar–R coupling product and the R–R sp^3-sp^3 coupling product should be less favorable, consistently with the selectivity observed for related group 10 metal complexes.[50]

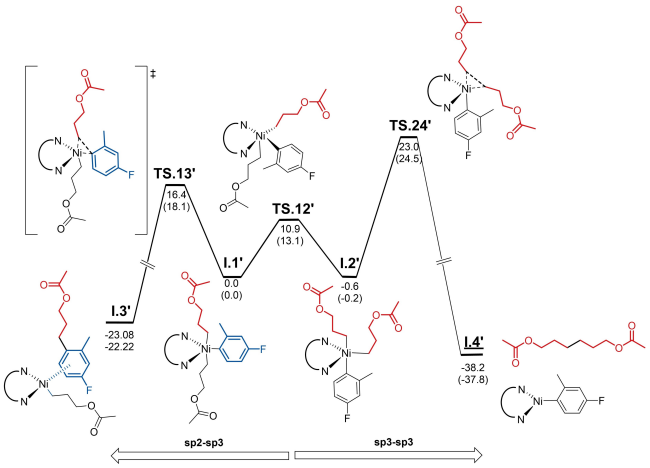

Figure 5. Computed relative ΔH (upper values) and ΔG (lower values) are reported in kcal.mol^{-1} for the two possible reductive elimination processes (sp^2-sp^3 and sp^3-sp^3) from $ArNi^{III}R_2$ (**I.1'**).

Discussion

Along with the choice of the photo- and organometallic catalysts, metallaphotocatalysis benefits from multiple parameters (stoichiometry of the reactants, spectrum of the light source, light intensity, concentration of the catalysts,.) to optimize its output. However, the kinetics governing the course of the photoconversion of the reactants is rather complex and optimization often requires more than intuition.

Hence, in this study, we departed from the wavelength of light excitation previously reported by us[12] upon considering a more favorable overlap with the absorption band of the photocatalyst and the reduction of photodegradation of an intermediate of the Ni catalytic cycle. Nevertheless, we observed a photoconversion, which proved less advantageous by requiring two equivalents of bis-(catecholato)silicate to yield the desired product. This rather unexpected result has pointed on the significance of two generally underestimated parameters driving metallaphotocatalysis: the spectrum of the light source (driving the k_e value; see Figure 4A) and the light intensity (driving the I_0 value; see Figure 4A). Thus, by using a powerful LED at 365 nm and by matching its spectrum with the absorption band of the iridium photocatalyst, we considerably increased the rate constant associated to the photocatalyst activation with respect to our previous investigation performed with a less powerful LED at 450 nm (see Supporting Information, Subsection 3.1). It correspondingly resulted in the production of Ir^{II} in high amount at steady-state. As a consequence, the Ir^{II}-mediated reduction of $ArNi^{III}BrR$ could significantly compete with the reductive elimination yielding Ar–R and $Ni^{I}Br$ (see Figures 4C–D), which diverting pathway was essentially absent in our original investigation.

Beyond this qualitative explanation, we could exploit our original approach of analytic derivation of the expressions of the photoconversion fluxes in order to quantitatively interpret the preceding results. Hence, whereas the condition $t_{switch} < t_{end}$ was most often met in the presently reported results obtained with the LED at 365 nm, we were in a regime where $t_{switch} > t_{end}$ in our previous series of experiments so as to observe only the first kinetic regime, corresponding to the most efficient product formation. In fact, the latter inequality amounts the ratio $[Ir]_0 \times I_0^{theo}/([Ni]_0)^2$ to remain smaller than the threshold value equal to $k_3/\beta k_e[R\text{–}Si^{\ominus}]_0$ estimated at 10^2 M^{-1} mW cm^{-2}, which points on the impact of the four control parameters $[Ir]_0$, I_0, and $[Ni]_0$, and $[R\text{–}Si^{\ominus}]_0$ for the reaction between Ar–Br and $R\text{–}Si^{\ominus}$ to be at the most efficient.

Conclusions

The C–C bond formation from an alkyl silicate and an aryl bromide under metallaphotoredox catalysis was thoroughly studied. The Ir cycle was investigated thanks to photophysical techniques and EPR, attesting a SET mechanism between the excited photocatalyst and the silicate to form the ligand-reduced Ir complex along with the alkyl radical. The study of the Ni cycle revealed an induction period when starting from $Ni^{II}Br_2$ to form the active Ni^0 species for the oxidative addition. The resulting $ArNi^{II}Br$ species, while being competent to trigger the catalytic cycle, was shown to trap an alkyl radical to form the Ar–R product after reductive elimination. These experimental results led us to propose a $Ni^0/Ni^{II}/Ni^{III}/Ni^{I}$ mechanism (path A, Scheme 1c). However due to the complexity of the system, classical approaches did not enable us to definitely reject path B, based on a $Ni^0/Ni^{I}/Ni^{III}/Ni^{I}$ mechanism. Thanks to a step-by-step micro-kinetics approach, we modeled different scenarios and determined the resting states for both catalysts. The careful analysis of the kinetic monitoring revealed two regimes for the formation of Ar–R at an appreciable rate. The first one could be modeled when considering an operative mechanism A but the sharp decrease of the reaction rate observed in the second phase, linked to an overconsumption of silicates, led us to propose an original scenario in which two alkyl silicates react when only one aryl bromide is transformed. When considering this second regime, the numerical

© 2023 Wiley-VCH GmbH

15213765, 0, Downloaded from https://chemistry-europe.onlinelibrary.wiley.com/doi/10.1002/chem.202301780 by Inrae - Dipso, Wiley Online Library on [17/10/2023]. See the Terms and Conditions (https://onlinelibrary.wiley.com/terms-and-conditions) on Wiley Online Library for rules of use; OA articles are governed by the applicable Creative Commons License

simulation of the mechanism proposed correctly fits the data and the mechanism was further supported by DFT calculations.

Moreover, this study provided general features to observe only the first regime, corresponding to the most efficient product formation. The analytic derivations to meet the corresponding condition $t_{switch} > t_{end}$ yields a ratio $[Ir]_0 \times I_0^{theo}/([Ni]_0)^2$ smaller than a threshold value equal to $k_3/\beta k_e[R\text{–}Si^{\ominus}]_0$, estimated at 10^2 $M^{-1}.mW.cm^{-2}$. Interestingly, the methodological developments previously reported by us[12] have been generally performed below this threshold by irradiating at 450 nm (blue LED) with an intensity around 30 times weaker than that used for the mechanistic study. In these conditions, the reaction between Ar–Br and R–$Si^{\ominus}$ proceeded smoothly and it turned out to be much more efficient than the same reaction performed at a wavelength suitably selected according to the photocatalyst properties.

To conclude, the combination of both analytical and numerical methods able to encompass multiple parameters proved to be of particular efficiency to decipher a complex mechanism such as this one. Yet, this case study also brings findings that go far beyond the context of the sole silicate/aryl bromide cross-coupling.

These include the reactivity of an $ArNi^{II}X$ complex under free radical conditions, the EPR characterization of a reduced iridium complex and its DFT modeling as well as the opportunity to use microkinetics to understand and minimize by-product formation.

Experimental Section

Chemicals: Reagents and solvents were purchased from commercial suppliers and used without further purification. Reactions were carried out under an argon atmosphere in oven dried glassware.

NMR: Spectra were recorded at ambient temperature on a Bruker Avance III Ultrashield™ 300 instrument. The ^1H NMR spectra were recorded at 300 MHz.^{13}C NMR spectra were recorded at 75 MHz. Chemical shifts (δ_H, δ_C) were quoted in parts per million (ppm) and were referenced to the residual solvent peak. The ^{19}F NMR spectra were recorded at 282 MHz with $CFCl_3$ as an external reference and fluorobenzene in a d6-DMSO insert for locking and as an internal standard.

Electrochemical experiments: Electrochemical experiments were performed under Ar flow in a three-electrode cell. The counter-electrode was a Pt wire of approximately 1 cm^2 apparent surface area, while the reference was a saturated calomel electrode separated from the solution by a bridge fulfilled with a 0.3 M of n-Bu_4NBF_4 in the desired solvent. The cyclic voltammograms (CV) were recorded at a steady glassy carbon disk (1/3 mm) using a potentiostat μ-autolab PGSTAT 101 from Metrohm using Nova 2.4 as software.

Light Sources: For analytical purposes, the experiments were carried out in NMR tubes submitted to both rotation for stirring (using a Roller oscillating roller mixer instrument) and illumination at $\lambda = 365$ nm with a homemade setup delivering light from blue LED at the NMR tubes (see Figure S1).

Spectroscopic measurements: The absorption spectra were recorded at 25 °C on a Cary 300 UV/Vis spectrophotometer (Agilent Technologies, Santa Clara, CA), equipped with a Peltier thermostated cell holder (t2x2 Sport/Cary300, Quantum Northwest, Liberty Lake, WA). The samples were placed in 2 mL quartz cuvettes (1 cm×1 cm light path; Hellma Optics, Jena, Germany).

The luminescence spectra were acquired on a LPS 220 spectrofluorometer (PTI, Monmouth Junction, NJ), equipped with a TLC50 cuvette holder (Quantum Northwest, Liberty Lake, WA) thermoregulated at 25 °C. The samples were placed in 2 mL quartz cuvettes (1 cm×1 cm light path; Hellma Optics, Jena, Germany).

The lifetime luminescence of $Ir^{(III)}$ was measured in the frequency-domain with the home-built setup shown in Scheme S1 by the phase-modulation method.

NMR monitoring of the time evolution of the system composition: The kinetic experiments have been carried out in NMR tubes at room temperature by using the home-built setup described in Figure S1 for stirring and irradiation at 365 nm. On average, a $^{19}F\{^1H\}$ NMR spectrum was recorded every 15 min. The peaks have been integrated and the information converted into concentration by using a solution of fluorobenzene in [*d6*]-DMSO contained in a coaxial insert for locking and as an internal standard for integration.

Variation of the nickel pre-catalyst: To an NMR tube was added R–$Si^{\ominus}$ (97 mg, 0.15 mmol, 1.5 equiv), Ir^{III} (2.2 mg, 2 mol%, 2 μmol), 4,4′-di-*tert*-butyl- 2,2′-bipyridine (1.07 mg, 4 mol%, 4 μmol) and $Ni^{II}Br_2$ (0.9 mg, 4 mol%, 4 μmol) or $Ni(COD)_2$ (1.1 mg, 4 mol%, 4 μmol) or $ArNi^{II}Br$ (2.06 mg, 4 mol%, 4 μmol) or $Ni^{I}Cl$ (3 mg, 4 mol%, 4 μmol). The tube was sealed with a rubber septum and evacuated/purged with vacuum/argon three times. Degassed DMF (1 mL) was introduced, followed by Ar–Br (13 μL, 0.1 mmol, 1 equiv) and the reaction mixture was irradiated at 365 nm for 4 h.

Kinetic simulation: All the computations were performed by using a python environment,[51,52] and were namely based on the scipy[53] and numpy[54] libraries for the numerical modelling. Standard algorithms for the integration of ordinary differential equations were used. Full data and python script are available in a separate archive file.

Evidence for the interaction between $ArNi^{II}Br$ and radicals: The ability of $ArNi^{II}Br$ to trap a free radical was assessed. For this purpose, $ArNi^{II}Br$ was heated at 80 °C with half an equivalent of dilauryl peroxide (DLP) in DMF. After 30 min, the 5-fluoro-2-undecyltoluene coupling product was observed by $^{19}F\{^1H\}$ NMR at −119.5 ppm in 70% yield (see Figure 2f). Its presence has been confirmed by mass spectrometry (see Figure S16).

Supporting Information

The authors have cited additional references within the Supporting Information.[55–65]

Acknowledgements

The authors thank Maxime R. Vitale, for fruitful discussions. L.F. thanks the Institut Universitaire de France. The authors thanks Sorbonne Université, CNRS and the ANR HyperSiLight, ANR-17-CE07-0018.

Conflict of Interest

The authors declare no conflict of interest.

Keywords: dual catalysis · mechanistic study · micro-kinetic modeling · nickel · photocatalysis

© 2023 Wiley-VCH GmbH

15213765, 0, Downloaded from https://chemistry-europe.onlinelibrary.wiley.com/doi/10.1002/chem.202301780 by Inrae - Dipso, Wiley Online Library on [17/10/2023]. See the Terms and Conditions (https://onlinelibrary.wiley.com/terms-and-conditions) on Wiley Online Library for rules of use; OA articles are governed by the applicable Creative Commons License

[1] J.-P Corbet, G. Mignani, *Chem. Rev.* **2006**, *106*, 2651–2710.
[2] A. Y. Chan, I. B. Perry, N. B. Bissonnette, B. F. Buksh, G. A. Edwards, L. I. Frye, O. L. Garry, M. N. Lavagnino, B. X. Li, Y. Liang, E. Mao, A. Millet, J. V. Oakley, N. L. Reed, H. A. Sakai, C. P. Seath, D. W. C. MacMillan, *Chem. Rev.* **2022**, *122*, 1485–1542.
[3] J. C. Tellis, C. B. Kelly, D. N. Primer, M. Jouffroy, N. R. Patel, G. A. Molander, *Acc. Chem. Res.* **2016**, *49*, 1429–1439.
[4] Z. Zuo, D. T. Ahneman, L. Chu, J. A. Terrett, A. G. Doyle, D. W. C. MacMillan, *Science* **2014**, *345*, 437–440.
[5] J. C. Tellis, D. N. Primer, G. A. Molander, *Science* **2014**, *345*, 433–436.
[6] T. Knauber, R. Chandrasekaran, J. W. Tucker, J. M. Chen, M. Reese, D. A. Rankic, N. Sach, C. Helal, *Org. Lett.* **2017**, *19*, 6566–6569.
[7] K. Nakajima, S. Nojima, Y. Nishibayashi, *Angew. Chem. Int. Ed.* **2016**, *55*, 14106–14110.
[8] C. H. Basch, J. Liao, J. Xu, J. J. Piane, M. P. Watson, *J. Am. Chem. Soc.* **2017**, *139*, 5313–5316.
[9] F. J. R. Klauck, M. J. James, F. Glorius, *Angew. Chem. Int. Ed.* **2017**, *56*, 12336–12339.
[10] L. Huang, T. Ji, M. Rueping, *J. Am. Chem. Soc.* **2020**, *142*, 3532–3539.
[11] a) C. Le, Y. F. Liang, R. W. Evans, X. M. Li, D. W. C. MacMillan, *Nature* **2017**, *547*, 79–83; b) I. B. Perry, T. F. Brewer, P. J. Sarver, D. M. Schultz, D. A. DiRocco, D. W. C. MacMillan, *Nature* **2018**, *560*, 70–75; c) M. H. Shaw, V. W. Shurtleff, J. A. Terrett, J. D. Cuthbertson, D. W. C. MacMillan, *Science* **2016**, *352*, 1304–1308.
[12] V. Corcé, L.-M. Chamoreau, E. Derat, J.-P. Goddard, C. Ollivier, L. Fensterbank, *Angew. Chem. Int. Ed.* **2015**, *54*, 11414–11418.
[13] C. Lévêque, L. Chenneberg, V. Corcé, J.-P. Goddard, C. Ollivier, L. Fensterbank, *Org. Chem. Front.* **2016**, *3*, 462–465.
[14] M. Jouffroy, D. N. Primer, G. A. Molander, *J. Am. Chem. Soc.* **2016**, *138*, 475–478.
[15] S. Biswas, D. J. Weix, *J. Am. Chem. Soc.* **2013**, *135*, 16192–16197.
[16] S. L. Zultanski, G. C. Fu, *J. Am. Chem. Soc.* **2013**, *135*, 624–627.
[17] O. Gutierrez, J. C. Tellis, D. N. Primer, G. A. Molander, M. C. Kozlowski, *J. Am. Chem. Soc.* **2015**, *137*, 4896–4899.
[18] M. Yuan, Z. Song, S. O. Badir, G. A. Molander, O. Gutierrez, *J. Am. Chem. Soc.* **2020**, *142*, 7225–7234.
[19] D. N. Primer, G. A. Molander, *J. Am. Chem. Soc.* **2017**, *139*, 9847–9850.
[20] B. Maity, C. Zhu, M. Rueping, L. Cavallo, *ACS Catal.* **2021**, *11*, 13973–13982.
[21] S. I. Ting, S. Garakyaraghi, C. M. Taliaferro, B. J. Shields, G. D. Scholes, F. N. Castellano, A. G. Doyle, *J. Am. Chem. Soc.* **2020**, *142*, 5800–5810.
[22] R. Sun, Y. Qin, S. Ruccolo, C. Schnedermann, C. Costentin, D. G. Nocera, *J. Am. Chem. Soc.* **2019**, *141*, 89–93.
[23] Y. Qin, R. Sun, N. P. Gianoulis, D. G. Nocera, *J. Am. Chem. Soc.* **2021**, *143*, 2005–2015.
[24] C. N. Prieto Kullmer, J. A. Kautzky, S. W. Krska, T. Nowak, S. D. Dreher, D. W. C. MacMillan *Science* **2022**, *376*, 532–539.
[25] See also with a phenanthroline ligand: Q. Lin, T. Diao, *J. Am. Chem. Soc.* **2019**, *141*, 17937–17948.
[26] Y. Kawamata, J. C. Vantourout, D. P. Hickey, P. Bai, L. Chen, Q. Hou, W. Qiao, K. Barman, M. A. Edwards, A. F. Garrido-Castro, J. N. deGruyter, H. Nakamura, K. Knouse, C. Qin, K. J. Clay, D. Bao, C. Li, J. T. Starr, C. Garcia-Irizarry, N. Sach, H. S. White, M. Neurock, S. D. Minteer, P. S. Baran, *J. Am. Chem. Soc.* **2019**, *141*, 6392–6402.
[27] N. A. Till, S. Oh, D. W. C. MacMillan, M. J. Bird, *J. Am. Chem. Soc.* **2021**, *143*, 9332–9337.
[28] S. I. Ting, W. L. Williams, A. G. Doyle, *J. Am. Chem. Soc.* **2022**, *144*, 5575–5582.
[29] Y. Ben-Tal, G. C. Lloyd-Jones, *J. Am. Chem. Soc.* **2022**, *144(33)*, 15372–15382.
[30] a) J. Chatt, B. L. Shaw, *J. Chem. Soc.* **1960**, 1718–1729; b) M. Hidai, T. Kashiwagi, T. Ikeuchi, Y. Uchida, *J. Organomet. Chem.* **1971**, *30*, 279–282; c) N. H. Park, G. Teverovskiy, S. L. Buchwald, *Org. Lett.* **2014**, *16*, 220–223.
[31] A genuine photoredox catalytic cycle was established for an allylation reaction of an alkylsilicate using 4CzIPN as photocatalyst, see: A. Cartier, E. Levernier, V. Corcé, T. Fukuyama, A.-L. Dhimane, C. Ollivier, I. Ryu, L. Fensterbank, *Angew. Chem. Int. Ed.* **2019**, *58*, 1789–1793.
[32] M. A. Cismesia, T. P. Yoon, *Chem. Sci.* **2015**, *6*, 5426–5434.
[33] D. Hartmann, T. Thorwart, R. Müller, J. Thusek, J. Schwabedissen, A. Mix, J. H. Lamm, B. Neumann, N. W. Mitzel, L. Greb, *J. Am. Chem. Soc.* **2021**, *143*, 18784–18793.
[34] B. J. Shields, B. Kudisch, G. D. Scholes, A. G. Doyle, *J. Am. Chem. Soc.* **2018**, *140*, 3035–3039.
[35] S. K. Kariofillis, A. G. Doyle, *Acc. Chem. Res.* **2021**, *54*, 988–1000.
[36] See also: D. R. Heitz, J. C. Tellis, G. A. Molander, *J. Am. Chem. Soc.* **2016**, *138*, 12715–12718.
[37] F. Strieth-Kalthoff, F. Glorius, *Chem* **2020**, *6*, 1888–1903.
[38] For a recent study, see: R. Kancherla, K. Muralirajan, B. Maity, S. Karudethat, G. S. Kumar, F. Laquai, L. Cavallo, M. Rueping, *Nat. Commun.* **2022**, *13*, 2737.
[39] D. Hanss, J. C. Freys, G. Bernardinelli, O. S. Wenger, *Eur. J. Inorg. Chem.* **2009**, 4850–4859.
[40] H. G. Roth, N. A. Romero, D. A. Nicewicz, *Synlett* **2016**, *27*, 714–723.
[41] S. I. Bokarev, D. Hollmann, A. Pazidis, A. Neubauer, J. Radnik, O. Kühn, S. Lochbrunner, H. Junge, M. Beller, A. Brückner, *Phys. Chem. Chem. Phys.* **2014**, *16*, 4789–4796.
[42] This CASSCF calculation done with the def2-TZVP basis set was used in conjunction with the DLPNO-NEVPT2 correction as implemented in ORCA version 4.1. Y. Guo, K. Sivalingam, E. F. Valeev, F. Neese, *J. Chem. Phys.* **2016**, *144*, 094111.
[43] G. R. Buettner, *Free Radical Biol. Med.* **1987**, *3*, 259–303.
[44] M. M. Beromi, G. W. Brudvig, N. Hazari, H. M. C. Lant, B. Q. Mercado, *Angew. Chem. Int. Ed.* **2019**, *131*, 6155–6159.
[45] M. Troupel, Y. Rollin, O. Sock, G. Meyer, J. Perichon, *New J. Chem.* **1986**, *10*, 593–599.
[46] K. Wang, Z. Ding, Z. Zhou, W. Kong, *J. Am. Chem. Soc.* **2018**, *140*, 12364–12368.
[47] R. S. Nicholson, I. Shain *Anal. Chem.* **1964**, *36*, 706–723.
[48] M. Durandetti, M. Devaud, J. Perichon, *New J. Chem.* **1996**, *20*, 659–667.
[49] a) S.-Z. Sun, Y. Duan, R. S. Mega, R. J. Somerville, R. Martin, *Angew. Chem. Int. Ed.* **2020**, *59*, 4370–4374; b) A. G. Bakhoda, S. Wiese, C. Greene, B. C. Figula, J. A. Bertke, T. H. Warren, *Organometallics* **2020**, *39*, 1710–1718; c) A. Vasilopoulos, S. W. Krska, S. S. Stahl, *Science* **2021**, *372*, 398–403.
[50] F. N. Hosseini, S. M. Nabavizadeh, R. Shoara, M. D. Aseman, M. M. Abu-Omar, *Organometallics* **2021**, *40*, 2051–2063.
[51] T. E. Oliphant, *Computing in Science Engineering* **2007**, *9*, 10–20.
[52] K. J. Millman, M. Aivazis, *Computing in Science Engineering* **2011**, *13*, 9–12.
[53] P. Virtanen, R. Gommers, T. E. Oliphant, M. Haberland, T. Reddy, D. Cournapeau, E. Burovski, P. Peterson, W. Weckesser, J. Bright, S. J. van der Walt, M. Brett, J. Wilson, K. J. Millman, N. Mayorov, A. R. J. Nelson, E. Jones, R. Kern, E. Larson, C. J. Carey, İ. Polat, Y. Feng, E. W. Moore, J. VanderPlas, D. Laxalde, J. Perktold, R. Cimrman, I. Henriksen, E. A. Quintero, C. R. Harris, A. M. Archibald, A. H. Ribeiro, F. Pedregosa, P. van Mulbregt, *SciPy 1.0 Contributors, Nat. Methods* **2020**, *17*, 261–272.
[54] S. van der Walt, S. C. Colbert, G. Varoquaux, *Computing in Science Engineering* **2011**, *13*, 22–30.
[55] A. Beeby, S. Bettington, I. J. S. Fairlamb, A. E Goeta, A. R. Kapdi, E. H. Niemelä, A. L. A. Thompson, *New J. Chem.* **2004**, *28*, 600–605.
[56] P. F. Wang, L. Jullien, B. Valeur, J.-S. Filhol, J. Canceill, J.-M. Lehn, *New J. Chem.* **1996**, *20*, 895–907.
[57] C. K. Prier, D. A. Rankic, D. W. C. MacMillan, *Chem. Rev.* **2013**, *113*, 5322–5363.
[58] F. Neese, Software Update: The ORCA Program System, Version 4.0. *WIREs Comput. Mol. Sci.* **2018**, *8*, e1327.
[59] A. Najibi, L. Goerigk, *J. Chem. Theory Comput.* **2018**, *14*, 5725–5738.
[60] A. D. Becke, *Phys. Rev. A* **1988**, *38*, 3098–3100.
[61] C. Lee, W. Yang, R. G. Parr, *Phys. Rev. B* **1988**, *37*, 785–789.
[62] J. P. Perdew, M. Ernzerhof, K. Burke, *J. Chem. Phys.* **1996**, *105*, 9982–9985.
[63] Y. Zhao, D. G. Truhlar, *Theor. Chem. Acc.* **2008**, *120*, 215–241.
[64] J. P Perdew, J. Tao, V. N. Staroverov, G. E. Scuseria, *J. Chem. Phys.* **2004**, *120*, 6898–6911.
[65] N. Ansmann, D. Hartmann, S. Sailer, P. Erdmann, R. Maskey, M. Schorpp, L. Greb, *Angew. Chem. Int. Ed.* **2022**, *61*, e202203947.

Manuscript received: June 3, 2023
Accepted manuscript online: July 26, 2023
Version of record online: ■■, ■■

© 2023 Wiley-VCH GmbH

15213765, 0, Downloaded from https://chemistry-europe.onlinelibrary.wiley.com/doi/10.1002/chem.202301780 by Inrae - Dipso, Wiley Online Library on [17/10/2023]. See the Terms and Conditions (https://onlinelibrary.wiley.com/terms-and-conditions) on Wiley Online Library for rules of use; OA articles are governed by the applicable Creative Commons License

Metallophotoredox catalyzed coupling of an aryl bromide with an alkyl bis(catecholato)silicate can lead to the formation of large quantity of side products when subjected to high intensity/high frequency irradiation. Two regimes were found to be possible; the ability to switch from the quantitative coupling to the simultaneous coupling and degradation of the silicate was observed.

Dr. K. Jaouadi, Dr. M. Abdellaoui, Dr. E. Levernier, Dr. P.-A. Payard, Dr. E. Derat, Dr. T. Le Saux, Dr. C. Ollivier, Dr. S. Torelli, Prof. L. Jullien, Dr. R. Plasson, Prof. L. Fensterbank*, Dr. L. Grimaud**

1 – 13

Regime Switch in the Dual-Catalyzed Coupling of Alkyl Silicates with Aryl Bromides

15213765, 0, Downloaded from https://chemistry-europe.onlinelibrary.wiley.com/doi/10.1002/chem.202301780 by Inrae - Dipso, Wiley Online Library on [17/10/2023]. See the Terms and Conditions (https://onlinelibrary.wiley.com/terms-and-conditions) on Wiley Online Library for rules of use; OA articles are governed by the applicable Creative Commons License